MODELING AND CONTROL OF A TILT-ROTOR UAV WITH IMPROVED FORWARD FLIGHT

Daniel Neri*, Guilherme V. Raffo*†, Sergio Esteban‡

*Graduate Program in Electrical Engineering, Federal University of Minas Gerais
Belo Horizonte, MG, Brazil

†Department of Electronic Engineering, Federal University of Minas Gerais
Belo Horizonte, MG, Brasil

‡Department of Aerospace Engineering, Universidad de Sevilla, Seville, Spain

Emails: `nericardoso@ufmg.br, raffo@ufmg.br, sesteban@us.es`

Abstract— This work describes the modeling and control of a tilt-rotor UAV with tail controlled surfaces for path tracking with improved forward velocity. The dynamic model is obtained using the Euler-Lagrange formulation. Mixed H_2/H_∞ controllers are designed for different operation points, whose feedback gains are interpolated by a neural network for online gain-scheduling, performing a smooth transition between them. Simulation results show the control strategy efficiency when the UAV is designated to have a forward acceleration and do a circular trajectory, subject to wind perturbation.

Keywords— UAV, Tilt-rotor, Robust control, Neural Network

Resumo— Esse trabalho descreve a modelagem e controle de um VANT tilt-rotor com superfícies de controle na cauda para realizar o seguimento de trajetória com aumento de velocidade de avanço. O modelo dinâmico é obtido usando a formulação de Euler-Lagrange. Através do projeto de controle H_2/H_∞ misto são obtidos ganhos de realimentação para diferentes pontos de operação, sendo esses interpolados por uma rede neural, para realizar um escalonamento online entre eles, permitindo uma transição suave. Resultados de simulação mostram a eficiência da estratégia de controle quando o VANT é designado a acelerar e seguir em uma trajetória circular com perturbação de vento.

Palavras-chave— UAV, Tilt-rotor, Controle robusto, Redes Neurais

1 Introduction

A tilt-rotor is a kind of aircraft that can perform vertical take-off and landing (VTOL) like rotary-wing airplanes, and at the same time, by tilting the rotors, can perform like a fixed-wing aircraft in forward flush, which substantially improves both performance and power consumption. Examples of tilt-rotors are the XV-15 (Nasa, 1975) and V-22 Osprey (Norton, 2004). These vehicles are ideal for some situations, since they do not need a wide area for take-off and landing. In small scale this UAV configuration can be used to perform, for example, bridge inspection looking for structural cracks, and search and rescue (Ryan and Hedrick, 2005). Moreover, due to its reduced number of rotors, these vehicles performing VTOL have the advantage, when compared to quad rotor UAV's, of lower energy consumption.

There are many works that propose control strategies for this class of UAV based on helicopter flight-mode model to solve the path tracking problem: PID (Papachristos, Alexis and Tzes, 2011), backstepping technique (Kendoul et al., 2005), linear model predictive controller (LMPC) (Papachristos, Alexis, Nikolakopoulos and Tzes, 2011), H_∞ with $D-$stability (Almeida, 2014), feedback linearization with PID (Almeida and Raffo, 2015); and robust linear mixed H_2/H_∞ optimal controller (Donadel et al., 2014). However, all these works neglected aerodynamic forces.

To improve the flight performance, tail surfaces are added to the UAV, since when it is in helicopter flight-mode (low velocity) the deflection of rudder or elevator do not produce significant effects, as opposed to in forward flights, where low deflection in these surfaces can make great difference in forces that act on the vehicle. Although the flight performance improvement is achieved with vertical tail plane (VTP) and horizontal tail plane (HTP), the control design becomes challenging. In this work we present an approach for dealing with this problem, by designing an adaptive controller based on online gain-scheduling using neural network (NN).

2 Modeling

This section develops the tilt-rotor UAV dynamic model using the Euler-Lagrange formulation.

2.1 Forward kinematics

The tilt-rotor UAV considered in this work is formed by three bodies. The main body is composed by the fuselage, horizontal and vertical stabilizer. The reminder two bodies are each of the two thruster's groups (servomotors with rotors) interconnected to the main body by revolute joints. In order to obtain the forward kinematics, seven frames are defined, as shown in Figure 1: the inertial frame $\mathcal{I}$; the body frame, $\mathcal{B}$; the main body center of mass $\mathcal{C}_1$; the two thruster's group center of mass, $\mathcal{C}_2$ and $\mathcal{C}_3$, correspondent to right and left sides, respectively, and the auxiliary frames $\mathcal{C}_2^{\text{aux}}$ and $\mathcal{C}_3^{\text{aux}}$.

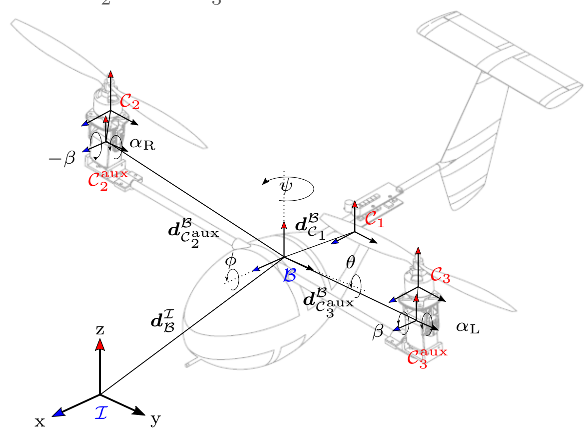

Figure 1: Tilt-rotor UAV frames.

The homogeneous transformation matrix from $\mathcal{B}$ to $\mathcal{I}$ is expressed as $\boldsymbol{H}^{\mathcal{I}}_{\mathcal{B}} = \begin{bmatrix} \boldsymbol{R}^{\mathcal{I}}_{\mathcal{B}} & \boldsymbol{d}^{\mathcal{I}}_{\mathcal{B}} \\ \boldsymbol{0}_{1\times3} & 1 \end{bmatrix}$, where $\boldsymbol{d}^{\mathcal{I}}_{\mathcal{B}} \triangleq \begin{bmatrix} x & y & z \end{bmatrix}'$ is the position of the origin of frame $\mathcal{B}$ with respect to $\mathcal{I}$, and $\boldsymbol{R}^{\mathcal{I}}_{\mathcal{B}} \triangleq \boldsymbol{R}_{z,\psi}\boldsymbol{R}_{y,\theta}\boldsymbol{R}_{x,\phi}$ is the rotation matrix.

The homogeneous transformation matrices $\boldsymbol{H}^{\mathcal{B}}_{\mathcal{C}_1}$, $\boldsymbol{H}^{\mathcal{B}}_{\mathcal{C}_2}$ and $\boldsymbol{H}^{\mathcal{B}}_{\mathcal{C}_3}$ are defined as

$$\boldsymbol{H}^{\mathcal{B}}_{\mathcal{C}_1} = \begin{bmatrix} \boldsymbol{I}_{3\times3} & \boldsymbol{d}^{\mathcal{B}}_{\mathcal{C}_1} \\ \boldsymbol{0}_{1\times3} & 1 \end{bmatrix},$$

$$\boldsymbol{H}^{\mathcal{B}}_{\mathcal{C}_2} = \begin{bmatrix} \boldsymbol{R}^{\mathcal{B}}_{\mathcal{C}_2^{\text{aux}}} & \boldsymbol{d}^{\mathcal{B}}_{\mathcal{C}_2^{\text{aux}}} \\ \boldsymbol{0}_{1\times3} & 1 \end{bmatrix} \begin{bmatrix} \boldsymbol{I}^{3\times3} & \boldsymbol{d}^{\mathcal{C}_2^{\text{aux}}}_{\mathcal{C}_2} \\ \boldsymbol{0}_{1\times3} & 1 \end{bmatrix},$$

$$\boldsymbol{H}^{\mathcal{B}}_{\mathcal{C}_3} = \begin{bmatrix} \boldsymbol{R}^{\mathcal{B}}_{\mathcal{C}_3^{\text{aux}}} & \boldsymbol{d}^{\mathcal{B}}_{\mathcal{C}_3^{\text{aux}}} \\ \boldsymbol{0}_{1\times3} & 1 \end{bmatrix} \begin{bmatrix} \boldsymbol{I}_{3\times3} & \boldsymbol{d}^{\mathcal{C}_3^{\text{aux}}}_{\mathcal{C}_3} \\ \boldsymbol{0}_{1\times3} & 1 \end{bmatrix},$$

where $\boldsymbol{R}^{\mathcal{B}}_{\mathcal{C}_2^{\text{aux}}} \triangleq \boldsymbol{R}_{x,-\beta}\boldsymbol{R}_{y,\alpha_R}$, $\boldsymbol{R}^{\mathcal{B}}_{\mathcal{C}_3^{\text{aux}}} \triangleq \boldsymbol{R}_{x,\beta}\boldsymbol{R}_{y,\alpha_L}$, β is a small inside inclination angle introduced to each of the propellers in order to improve the system controllability (Raffo, 2011), α_{R} and α_{L} are the right and left servomotor's rotation angles, respectively [1], $\boldsymbol{I}_{n\times n} \in R^{n\times n}$ is an identity matrix, and $\boldsymbol{0}_{n\times m} \in R^{n\times m}$ is a matrix of zeros.

Using $\boldsymbol{H}^{\mathcal{I}}_{\mathcal{B}}$, $\boldsymbol{H}^{\mathcal{B}}_{\mathcal{C}_1}$, $\boldsymbol{H}^{\mathcal{B}}_{\mathcal{C}_2}$ and $\boldsymbol{H}^{\mathcal{B}}_{\mathcal{C}_3}$, the homogeneous transformation matrices associated to the three centers of mass are obtained as $\boldsymbol{H}^{\mathcal{I}}_{\mathcal{C}_1} = \boldsymbol{H}^{\mathcal{I}}_{\mathcal{B}}\boldsymbol{H}^{\mathcal{B}}_{\mathcal{C}_1}$, $\boldsymbol{H}^{\mathcal{I}}_{\mathcal{C}_2} = \boldsymbol{H}^{\mathcal{I}}_{\mathcal{B}}\boldsymbol{H}^{\mathcal{B}}_{\mathcal{C}_2}$ and $\boldsymbol{H}^{\mathcal{I}}_{\mathcal{C}_3} = \boldsymbol{H}^{\mathcal{I}}_{\mathcal{B}}\boldsymbol{H}^{\mathcal{B}}_{\mathcal{C}_3}$, where $\boldsymbol{H}^{\mathcal{I}}_{i} = \begin{bmatrix} \boldsymbol{R}^{\mathcal{I}}_{i} & \boldsymbol{p}^{\mathcal{I}}_{i} \\ \boldsymbol{0}_{1\times3} & 1 \end{bmatrix}$, with $\boldsymbol{p}^{\mathcal{I}}$ and $\boldsymbol{R}^{\mathcal{I}}_i$ being the position and the rotation matrix of frame $i = \{\mathcal{C}_1, \mathcal{C}_2, \mathcal{C}_3\}$ with respect to $\mathcal{I}$.

The Jacobian matrices of linear, $\boldsymbol{J}_i$, and angular, $\boldsymbol{W}_i$, velocities, from frame i with respect to $\mathcal{I}$, are obtained through the position vector time derivative, $\boldsymbol{v}^{\mathcal{I}}_i = d\boldsymbol{p}^{\mathcal{I}}_i/dt = \boldsymbol{J}_i\dot{\boldsymbol{q}}$, and the rotational matrix one, $\dot{\boldsymbol{R}}^{\mathcal{I}}_i = \boldsymbol{S}(\boldsymbol{w}^{\mathcal{I}}_{\mathcal{I},i})\boldsymbol{R}^{\mathcal{I}}_i$, where $\boldsymbol{S}(\boldsymbol{w}^{\mathcal{I}}_{\mathcal{I},i})$ is a skew-symmetric matrix. From the latter the angular center of mass velocity vector, $\boldsymbol{w}^{\mathcal{I}}_{\mathcal{I},i} = \boldsymbol{W}_i\dot{\boldsymbol{q}}$, is computed. Besides, $\boldsymbol{v}^{\mathcal{I}}_i \in R^{3\times1}$ is the linear center of mass velocity vector, and $\boldsymbol{q} \triangleq \begin{bmatrix} x & y & z & \phi & \theta & \psi & \alpha_R & \alpha_L \end{bmatrix}'$ is the generalized coordinates vector (Spong et al., 2006).

[1] Throughout the article subscripts L and R will be used to differentiate between the left and right components of the thruster's groups.

2.2 Euler-Lagrange dynamic model

The Euler-Lagrange formulation uses total kinetic and potential energy to obtain the system's equations of motion in the canonical form

$$\boldsymbol{M}(\boldsymbol{q})\ddot{\boldsymbol{q}} + \boldsymbol{C}(\boldsymbol{q},\dot{\boldsymbol{q}})\dot{\boldsymbol{q}} + \boldsymbol{g}(\boldsymbol{q}) = \boldsymbol{\vartheta}(\dot{\boldsymbol{q}},\boldsymbol{q},\boldsymbol{u},\boldsymbol{w}), \quad (1)$$

where $\boldsymbol{M}(\boldsymbol{q}) \in R^{8\times8}$ and $\boldsymbol{C}(\boldsymbol{q},\dot{\boldsymbol{q}}) \in R^{8\times8}$ are the inertia and Coriolis matrices, $\boldsymbol{g}(\boldsymbol{q})$ is the gravitational vector, and $\boldsymbol{\vartheta}(\dot{\boldsymbol{q}},\boldsymbol{q},\boldsymbol{u},\boldsymbol{w})$ are the generalized forces that act in the system (Spong et al., 2006). The generalized forces are functions of the disturbance vector $\boldsymbol{w}$ and control inputs vector $\boldsymbol{u}$. In this work $\boldsymbol{u} = \begin{bmatrix} f_{p_R} & f_{p_L} & \tau_{p_R} & \tau_{p_L} & \delta_e & \delta_r \end{bmatrix}'$, with f_{p_R} and f_{p_L} being the forces generated by the propellers, τ_{p_R} and τ_{p_L} the torques applied by the servomotors, and δ_e and δ_r the elevator and rudder deflection.

The inertia matrix is obtained from the kinetic energy $\mathcal{K} = (1/2)\dot{\boldsymbol{q}}'\boldsymbol{M}(\boldsymbol{q})\dot{\boldsymbol{q}}$, with $\boldsymbol{M}(\boldsymbol{q}) = \left[\sum_{i=1}^{3} m_i\boldsymbol{J}_i'\boldsymbol{J}_i + \boldsymbol{W}_i'\boldsymbol{R}^{\mathcal{I}}_i\boldsymbol{I}_i(\boldsymbol{R}^{\mathcal{I}}_i)'\boldsymbol{W}_i\right]$, where $m_i \in R$ and $\boldsymbol{I}_i \in R^{3\times3}$ represent the i-th body mass and inertia tensor matrix, respectively. Using the inertia matrix, the Coriolis matrix is obtained by the Christofell symbols of first kind as

$$C_{kj} = \sum_{l=1}^{8} \frac{1}{2}\left[\frac{\partial \boldsymbol{M}_{kj}}{\partial \boldsymbol{q}_l} + \frac{\partial \boldsymbol{M}_{kl}}{\partial \boldsymbol{q}_j} - \frac{\partial \boldsymbol{M}_{lj}}{\partial \boldsymbol{q}_k}\right],$$

where C_{kj} is an element of the Coriolis matrix.

The gravitational force vector is obtained by $\boldsymbol{g}(\boldsymbol{q}) = \partial\mathcal{U}/\partial\boldsymbol{q}$, where $\mathcal{U} = -\sum_{i=1}^{3} m_i\boldsymbol{g}_{\boldsymbol{r}}'\boldsymbol{p}^{\mathcal{I}}_i$, with $\boldsymbol{g}_{\boldsymbol{r}}'$ being the gravity acceleration vector.

2.3 Generalized forces

The vector of generalized forces $\boldsymbol{\vartheta} \in \mathcal{R}^{8\times1}$ in equation (1) is composed by generalized forces applied by the propellers, servomotors and aerodynamic surfaces

$$\boldsymbol{\vartheta} = \boldsymbol{\vartheta}_{P_R} + \boldsymbol{\vartheta}_{P_L} + \boldsymbol{\vartheta}_{s_R} + \boldsymbol{\vartheta}_{s_L} + \boldsymbol{\vartheta}_f + \boldsymbol{\vartheta}_h + \boldsymbol{\vartheta}_v, \quad (2)$$

where $\boldsymbol{\vartheta}_{P_R}$ and $\boldsymbol{\vartheta}_{P_L}$ are generalized forces generated by propellers, $\boldsymbol{\vartheta}_{s_R}$ and $\boldsymbol{\vartheta}_{s_L}$ are applied by servomotors, and $\boldsymbol{\vartheta}_f$, $\boldsymbol{\vartheta}_h$ and $\boldsymbol{\vartheta}_v$ are generated by the fuselage and the horizontal and vertical stabilizers, respectively.

The forces and torques contributions are added using the maps $\boldsymbol{\vartheta}_f = (\boldsymbol{J}_p)'f^{\mathcal{I}}$ and $\boldsymbol{\vartheta}_\tau = (\boldsymbol{W}_{\mathcal{F}})'\tau^{\mathcal{I}}$ (Kane and Levinson, 1985), where $\boldsymbol{J}_p$ is the linear velocity jacobian associated to the force application point, and $\boldsymbol{W}_{\mathcal{F}}$ is the angular velocity jacobian of the body with attached frame $\mathcal{F}$, to which the torque is applied. The terms $f^{\mathcal{I}}$ and $\tau^{\mathcal{I}}$ are the applied force and torque, represented in the inertial frame.

The propellers contribution to the generalized forces are obtained as

$$\boldsymbol{\vartheta}_{P_R}=\boldsymbol{J}'_{C_2}\boldsymbol{R}^{\mathcal{I}}_{C_2}\begin{bmatrix}\mathbf{0}_{2\times1}\\ f_{z_R}\end{bmatrix}+\boldsymbol{W}'_{C_2}\boldsymbol{R}^{\mathcal{I}}_{C_2}\begin{bmatrix}\mathbf{0}_{2\times1}\\ \frac{k_\tau}{b}f_{z_R}\end{bmatrix}, \quad (3)$$

$$\boldsymbol{\vartheta}_{P_L}=\boldsymbol{J}'_{C_3}\boldsymbol{R}^{\mathcal{I}}_{C_3}\begin{bmatrix}\mathbf{0}_{2\times1}\\ f_{z_L}\end{bmatrix}+\boldsymbol{W}'_{C_3}\boldsymbol{R}^{\mathcal{I}}_{C_3}\begin{bmatrix}\mathbf{0}_{2\times1}\\ -\frac{k_\tau}{b}f_{z_L}\end{bmatrix}, \quad (4)$$

in which the applied torque by the propeller is approximated assuming the rotor in steady-state (Castillo et al., 2005). The terms k_τ and b are constants that must be estimated; besides, it is considered that the propellers forces and torques are applied to the centers of mass of the thrusters group.

The generalized torques applied by the servomotors are added as $\boldsymbol{\vartheta}_{s_R}=\begin{bmatrix}\mathbf{0}_{1\times6} & \tau_{P_R} & 0\end{bmatrix}'$ and $\boldsymbol{\vartheta}_{s_L}=\begin{bmatrix}\mathbf{0}_{1\times6} & 0 & \tau_{P_L}\end{bmatrix}'$.

As show in Stevens and Lewis (1992) and Beard and Mclain (2012), an airfoil in presence of a free-stream produces two orthogonal forces: lift, which is perpendicular to the free-stream, and drag, which is parallel to it. This work decomposes the wind-speed in $x{-}z$ and $x{-}y$ planes. Its magnitude is computed as $v_{a_{xy}}=\sqrt{(w{-}w_a)^2{+}(u{-}u_a)^2}$, $v_{a_{xz}}=\sqrt{(v-v_a)^2{+}(u-u_a)^2}$, where $\boldsymbol{w}{=}[u_a\ v_a\ w_a]'$ is the wind-speed components vector, due to environment, represented in the body frame, and it is treated as perturbation. Using the angle of attack, α_a, and side slip angle, β_a, computed as $\alpha_a{=}{-}tan^{-1}\left((w-w_a)/(u-u_a)\right)$, $\beta_a{=}-tan^{-1}\left((v-v_a)/(u-u_a)\right)$, it is possible to define the wind-speed orientation.

The aerodynamic forces due to the fuselage, represented in the body frame, are calculated as $\boldsymbol{f}^f{=}\boldsymbol{R}^{\mathcal{B}}_{\alpha}[-\nu^f_{xz}c^f_{d_{xz}}\ 0\ \nu^f_{xz}c^f_{l_{xz}}]'{+}\boldsymbol{R}^{\mathcal{B}}_{\beta}[-\nu^f_{xy}c^f_{d_{xy}}\ \nu^f_{xy}c^f_{l_{xy}}\ 0]'$, where $\nu^{\bar{k}}_{\bar{j}}\triangleq(1/2)\rho s^{\bar{k}}v^2_{a_{\bar{j}}}$, $\boldsymbol{R}^{\mathcal{B}}_{\alpha}\triangleq\boldsymbol{R}_{y,\alpha_a}$ and $\boldsymbol{R}^{\mathcal{B}}_{\beta}\triangleq\boldsymbol{R}_{z,\beta_a}$, the terms $c^{\bar{k}}_{d_{\bar{j}}}, c^{\bar{k}}_{l_{\bar{j}}}$ are drag and lift coefficients for $\bar{k}\in\{f,h,v\}$ and $\bar{j}=\{xz,xy\}$, ρ is the air density, and $s^{\bar{k}}$ is the surface area. The coefficients depend of the aerodynamic properties and are obtained from flow simulations.

The aerodynamic forces, represented in the body frame, due to the horizontal stabilizer are calculated as $\boldsymbol{f}^h=R^{\mathcal{B}}_{\alpha}[-\nu^h_{xz}c^h_{d_{xz}}\ 0\ \nu^h_{xz}\left[c^h_{l_{xz}}+c^e\right]]'$. Moreover, the aerodynamic forces acting on the aircraft due to the vertical stabilizer are given by $\boldsymbol{f}^v=R^{\mathcal{B}}_{\beta}[-\nu^v_{xy}c^v_{d_{xy}}\ \nu^v_{xy}\left[c^v_{l_{xy}}+c^r\right]\ 0]$, where $c^{\bar{i}}$ for $\bar{i}\in\{e,r\}$ are the elevator and rudder coefficients.

The aerodynamic generalized forces are calculated as $\boldsymbol{\vartheta}_f=\boldsymbol{J}_f{}'\boldsymbol{R}^{\mathcal{I}}_{\mathcal{B}}\ f^f$, $\boldsymbol{\vartheta}^{\mathrm{h}}=\boldsymbol{J}_h{}'\boldsymbol{R}^{\mathcal{I}}_{\mathcal{B}}\ f^h$ and $\boldsymbol{\vartheta}^{\mathrm{v}}=\boldsymbol{J}_v{}'\boldsymbol{R}^{\mathcal{I}}_{\mathcal{B}}\ f_v$, where the linear velocity jacobians $\boldsymbol{J}_f$, $\boldsymbol{J}_h$ and $\boldsymbol{J}_v$ are obtained from $d\boldsymbol{p}^{\mathcal{I}}_{\bar{k}}/dt=\boldsymbol{J}_{\bar{k}}\dot{\boldsymbol{q}}$, where $\boldsymbol{p}^{\mathcal{I}}_{\bar{k}}$ comes from $\boldsymbol{H}^{\mathcal{B}}_{\bar{k}}\triangleq\boldsymbol{H}^{\mathcal{I}}_{\mathcal{B}}\begin{bmatrix}\boldsymbol{I}_{3\times3} & \boldsymbol{d}^{\mathcal{B}}_{\bar{k}}\\ \mathbf{0}_{1\times3} & 1\end{bmatrix}=\begin{bmatrix}\boldsymbol{R}^{\mathcal{I}}_{\mathcal{B}} & \boldsymbol{p}^{\mathcal{I}}_{\bar{k}}\\ \mathbf{0}_{1\times3} & 1\end{bmatrix}$. The tilt-rotor UAV physical parameters are shown in Table 1.

2.4 Mapping of the body's velocities

To reduce the computational complexity of the Euler-Lagrange model, a mapping of the generalized velocities to the body's velocities is performed as $\hat{\boldsymbol{q}}=\boldsymbol{\Lambda}^{-1}\dot{\boldsymbol{q}}$, where $\hat{\boldsymbol{q}}\triangleq[u\ \ v\ \ w\ \ p\ \ q\ \ r\ \ \dot{\alpha_r}\ \ \dot{\alpha_l}]'$, $\boldsymbol{\Lambda}^{-1}=\text{blkdiag}\left((\boldsymbol{R}^{\mathcal{I}}_{\mathcal{B}})',\boldsymbol{W}_\eta,\boldsymbol{I}_{\mathbf{2\times2}}\right)$, and $\boldsymbol{W_\eta}=\begin{bmatrix}1 & 0 & -\sin(\theta)\\ 0 & \cos(\phi) & \cos(\theta)\sin(\phi)\\ 0 & -\sin(\phi) & \cos(\phi)\cos(\theta)\end{bmatrix}$. The time derivative is obtained from $\ddot{\boldsymbol{q}}{=}\dot{\boldsymbol{\Lambda}}\hat{\boldsymbol{q}}{+}\boldsymbol{\Lambda}\dot{\hat{\boldsymbol{q}}}$. Replacing the latter in (1), the model is rewritten as $\dot{\boldsymbol{\Lambda}}\hat{\boldsymbol{q}}{+}\boldsymbol{\Lambda}\dot{\hat{\boldsymbol{q}}}{=}\boldsymbol{M}(\boldsymbol{q})^{-1}\left[\boldsymbol{\vartheta}{-}\boldsymbol{g}(\boldsymbol{q}){-}\boldsymbol{C}(\boldsymbol{q},\boldsymbol{\Lambda}\hat{\boldsymbol{q}})\boldsymbol{\Lambda}\hat{\boldsymbol{q}}\right]$, yielding to

$$\begin{bmatrix}\dot{\boldsymbol{q}}\\ \dot{\hat{\boldsymbol{q}}}\end{bmatrix}=\begin{bmatrix}\boldsymbol{\Lambda}\hat{\boldsymbol{q}}\\ \boldsymbol{\Lambda}^{-1}\left[-\dot{\boldsymbol{\Lambda}}\hat{\boldsymbol{q}}+\boldsymbol{M}(\boldsymbol{q})^{-1}\boldsymbol{\Omega}\right]\end{bmatrix}, \quad (5)$$

where $\boldsymbol{\Omega}\triangleq\boldsymbol{\vartheta}-\boldsymbol{g}(\boldsymbol{q})-\boldsymbol{C}(\boldsymbol{q},\boldsymbol{\Lambda}\hat{\boldsymbol{q}})\boldsymbol{\Lambda}\hat{\boldsymbol{q}}$.

3 Control Strategy

Since the aerodynamic forces are proportional to the square of the aerodynamic velocity, during hover flight, the horizontal and vertical stabilizer do not produce significant forces, and both the longitudinal and directional control need to be performed with the thrusters' groups. This changes during forward flight, where both longitudinal and directional control is conducted using both the horizontal and vertical stabilizer rather than using the rotors. This posses a challenge regarding the nonlinearity of control selection that is hard to deal using a simple linear controller. In this work we propose an adaptive controller based on gain-scheduling to solve the path tracking problem.

Robust mixed H_2/H_∞ controllers are developed to stabilize the altitude and attitude for different operation points, providing also disturbance rejection with an improved transient response. In addition, based on the current state of the system, a neural network is used to schedule the synthesized controllers, by interpolating their gains, considering the neural network learn and generalized factor (Haykin, 2001), providing an online smooth transition between controllers. Furthermore, a kinematic controller is designed to the translational control. The control structure is illustrated in Figure 2.

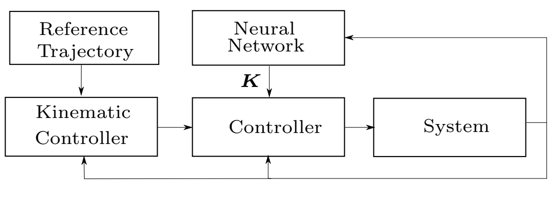

Figure 2: Control strategy scheme.

The system (5) is partitioned, from which the following model is considered for control design purposes

$$\dot{\boldsymbol{x}} = \begin{bmatrix} \dot{\hat{\boldsymbol{q}}} \\ \dot{\tilde{\boldsymbol{q}}} \end{bmatrix} = \boldsymbol{h}(\tilde{\boldsymbol{q}}, \hat{\boldsymbol{q}}, \boldsymbol{u}, \boldsymbol{w}), \tag{6}$$

where $\boldsymbol{x} = [\hat{\boldsymbol{q}} \ \tilde{\boldsymbol{q}}]'$ with $\tilde{\boldsymbol{q}} = [z \ \phi \ \theta \ \psi \ \alpha_R \ \alpha_L]'$. Using a first order Taylor series approximation, $\boldsymbol{A} = \partial\boldsymbol{h}/\partial\boldsymbol{x}$, $\boldsymbol{B}_u = \partial\boldsymbol{h}/\partial\boldsymbol{u}$, $\boldsymbol{B}_w = \partial\boldsymbol{h}/\partial\boldsymbol{w}$ for $\boldsymbol{x} = \boldsymbol{x}_{op}$, $\boldsymbol{u} = \boldsymbol{u}_{op}$ and $\boldsymbol{w} = \boldsymbol{0}_{3\times1}$ are obtained, and the linear system around an operation point is given by

$$\dot{\boldsymbol{x}} = \boldsymbol{A}\Delta\boldsymbol{x} + \boldsymbol{B}_u\Delta\boldsymbol{u} + \boldsymbol{B}_w\boldsymbol{w}, \tag{7}$$

where $\Delta \triangleq (.) - (.)_{\mathrm{op}}$, and "op" denotes the operation point.

The state-space error vector is augmented with integral action for some states to provide constant disturbance rejection and improve the closed-loop system performance. The closed-loop states vector is $\hat{\boldsymbol{x}} = \left[\Delta\hat{\boldsymbol{q}} \ \Delta\tilde{\boldsymbol{q}} \int \Delta z \ \int \Delta u \ \int \Delta v \ \int \Delta\psi\right]'$.

3.1 Robust Control Design

The inner-loop controllers, for the chosen operation points, are designed using the mixed H_2/H_∞ control law technique based on the following system (Donadel et al., 2014)

$$\begin{aligned} \dot{\hat{\boldsymbol{x}}}(t) &= \boldsymbol{A}\Delta\hat{\boldsymbol{x}}(t) + \boldsymbol{B}_u\Delta\boldsymbol{u}(t) + \boldsymbol{B}_w\boldsymbol{w}(t), \\ \boldsymbol{z}(t) &= \boldsymbol{C}_z\Delta\hat{\boldsymbol{x}}(t) + \boldsymbol{D}_{uz}\Delta\boldsymbol{u}(t) + \boldsymbol{D}_{wz}\boldsymbol{w}(t), \\ \boldsymbol{u}(t) &= \boldsymbol{K}\Delta\hat{\boldsymbol{x}}(t), \end{aligned} \tag{8}$$

where $\boldsymbol{C}_z$, $\boldsymbol{D}_{uz}$ and $\boldsymbol{D}_{wz}$ are constant matrices that must be adjusted.

The optimal H_∞ controller asymptotically stabilizes the linear system and minimizes the H_∞ norm, $||\boldsymbol{H}_{wz}(s)||_\infty = sup(\sigma\boldsymbol{H}_{wz}(jw))$, where $\boldsymbol{H}_{wz}(s)$ is the transfer function between the external disturbance $\boldsymbol{w}(t)$ and the cost variables $\boldsymbol{z}(t)$. Applying the Parseval theorem results in $||\boldsymbol{z}(t)||_2 \leq ||\boldsymbol{H}_{wz}(s)||_\infty ||\boldsymbol{w}(t)||_2$, in which clearly minimizing the H_∞ norm minimizes the disturbance effect on the system. In this work, differences between the linear model used for designing the controller and the real one is treated as perturbations. To solve the H_∞ problem, the following optimization problem subject to LMIs is considered

$$min \ \gamma, \quad \text{s.t.}$$

$$\boldsymbol{Q} > 0 \tag{9}$$

$$\begin{bmatrix} \boldsymbol{\Upsilon} & \boldsymbol{B}_w & \boldsymbol{Q}\boldsymbol{C}_z' + \boldsymbol{Y}'\boldsymbol{D}_{uz}' \\ * & -\gamma\boldsymbol{I}_{n_w\times n_w} & \boldsymbol{D}_{wz}' \\ * & * & -\gamma\boldsymbol{I}_{n_z\times n_z} \end{bmatrix} < 0 \tag{10}$$

$$\boldsymbol{L}\otimes\boldsymbol{Q} + \boldsymbol{M}\otimes\boldsymbol{\Gamma} + \boldsymbol{M}'\otimes\boldsymbol{\Gamma}' < 0, \tag{11}$$

where $\boldsymbol{\Gamma} = (\boldsymbol{A}\boldsymbol{Q}+\boldsymbol{B}_u\boldsymbol{Y})$, $\boldsymbol{\Upsilon} = \boldsymbol{A}\boldsymbol{Q} + \boldsymbol{Q}\boldsymbol{A}' + \boldsymbol{B}_u\boldsymbol{Y} + \boldsymbol{Y}'\boldsymbol{B}_u'$, the $*$ terms are used due to the matrix symmetry, and $\otimes$ is the Kronecker product. The constraint (11), with $\boldsymbol{L} = \begin{bmatrix} -r_a & c \\ c & r_a \end{bmatrix}$ and $\boldsymbol{M} = \begin{bmatrix} 0 & 1 \\ 0 & 0 \end{bmatrix}$, limits the pole allocation space by a circle of radius r_a and center c. Solving the optimization problem, the linear system will be asymptotically stable with feedback gain $\boldsymbol{K} = \boldsymbol{Y}\boldsymbol{Q}^{-1}$ and with H_∞ norm bounded by $||\boldsymbol{H}_{wz}(s)||_\infty < \sqrt{\gamma^*}$, where γ^* is the optimal value obtained from the optimization problem.

Consider again the system (8) with $\boldsymbol{D}_{wz} = 0$. The H_2 norm can be seen as the system impulse response, $||\boldsymbol{h}(t)||_2 = \int_0^\infty \boldsymbol{h}^2(t)dt$ for $\boldsymbol{h}(t) = \mathcal{L}^{-1}\{\boldsymbol{H}_{wz}(s)\}$. Minimizing this norm will provide an improved transient response of the system. The mixed H_2/H_∞ controller idea is to find an optimal H_∞ index γ^* and use $\hat{\gamma} > \gamma^*$ to solve the H_2 problem, maintaining H_∞ constraints; providing the advantage of a small H_∞ norm and a better transient response.

To solve the mixed H_2/H_∞ control problem, the following optimization problem must be considered for $\gamma = \hat{\gamma}$.

$$min \ tr(\boldsymbol{N}), \quad \text{s.t.}$$

$$\begin{bmatrix} \boldsymbol{N} & (\boldsymbol{C}_z + \boldsymbol{D}_{uz}\boldsymbol{K})\boldsymbol{Q} \\ \boldsymbol{Q}(\boldsymbol{C}_z + \boldsymbol{D}_{uz}\boldsymbol{K})' & \boldsymbol{Q} \end{bmatrix} > 0$$

$$\boldsymbol{Q}\boldsymbol{A}' + \boldsymbol{A}\boldsymbol{Q} + \boldsymbol{Y}'\boldsymbol{B}_u' + \boldsymbol{B}_u\boldsymbol{Y} + \boldsymbol{B}_w\boldsymbol{B}_w' < 0$$

$$\text{Constraints (9), (10) and (11)}$$

3.2 Gain-scheduling using neural network

A neural network called multilayer perceptron (MLP) with one hidden layer and one output layer is used to interpolate the controllers. To train the neural network some considerations are used: i) if the hidden layer has many neurons, the interpolation can perform curves between gains, which is not desired; ii) if the number of neurons in the hidden layer is not enough, the interpolation is not sufficiently adjusted to solve the problem; and iii) the more operating points are considered more controllers are tuned, which leads to an improvement of the neural network adjustment.

3.3 Kinematic Controller

The kinematic controller is designed to perform path tracking of the x-y motion by using a proportional controller with feed-forward term, which is given by

$$\begin{bmatrix} u_{r_k} \\ v_{r_k} \\ w_{r_k} \end{bmatrix} = \begin{bmatrix} k_u & 0 & 0 \\ 0 & k_v & 0 \\ 0 & 0 & k_w \end{bmatrix} (\boldsymbol{R}_{\mathcal{B}}^{\mathcal{I}})' \begin{bmatrix} x_r - x \\ y_r - y \\ 0 \end{bmatrix} + \begin{bmatrix} u_r \\ v_r \\ w_r \end{bmatrix}, \tag{12}$$

where u_r, v_r, w_r, x_r, y_r and z_r are the trajectory reference variables.

4 Results

In this section some results are presented to illustrate the controller efficiency. The system was linearized around three operation points: $\boldsymbol{x}_{op_1} = [0 \ \boldsymbol{0}_{9\times1} \ -0.0522 \ 0 \ 0.0520 \ 0.0520]$, $\boldsymbol{u}_{op_1} = [9.01 \ \ 9.01 \ \ 2.62.10^{-5} \ \ 2.62.10^{-5} \ \ 0 \ \ 0]$; $\boldsymbol{x}_{op_2} =$

$[6\ \ 0\ \ -0.3123\ \ \mathbf{0}_{7\times1}\ \ -0.0522\ \ 0\ \ 0.0546\ \ 0.0546]$, $\boldsymbol{u}_{op_2} = [9.01\ \ 9.01\ \ -1.44.10^{-4}\ \ -1.44.10^{-4}\ \ -0.158\ \ 0]$; and $\boldsymbol{x}_{op_3} = [12\ \ 0\ \ -0.6246\ \ \mathbf{0}_{7\times1}\ \ -0.0522\ \ 0\ \ 0.0624\ \ 0.0624]$, $\boldsymbol{u}_{op_3} = [9.02\ \ 9.02\ \ -6.59.10^{-4}\ \ -6.59.10^{-4}\ \ -0.158\ \ 0]$. The H_∞ optimization problem was solved using the yalmip MATLAB© toolbox, with the solver Lmilab, for $r_a = 100$, $c = 0$, and $\boldsymbol{C}_z$, $\boldsymbol{D}_{uz}$, $\boldsymbol{D}_{wz}$ adjusted as shown in (13), (14) and (15) for the three linear systems. An optimal γ^* was obtained and a $\hat{\gamma} = \gamma^* + 10$ was used to solve the mixed H_2/H_∞ problem. The obtained controller feedback gains $\boldsymbol{K}_1$, $\boldsymbol{K}_2$, $\boldsymbol{K}_3 \in R^{6\times18}$ are transformed in vectors $\boldsymbol{k}_1$, $\boldsymbol{k}_2$ and $\boldsymbol{k}_3 \in R^{108\times1}$ and used to train the neural network. The neural network inputs are the forward velocity operation-points values $u_{op_1} = 0\ m/s$, $u_{op_2} = 6\ m/s$ and $u_{op_3} = 12\ m/s$. A neural network MLP was configured with 4 neurons in the hidden layer with hyperbolic tangent activation function, and 108 neurons in the output layer with linear activation function. The neural network was trained using the Bayesian regularization backpropagation with 100 epochs, which produces an interpolation MSE (Mean Square Error) $3.57.10^{-8}$. The kinematic controller (12) was adjusted with $k_u = 0.1$, $k_v = 0.04$, and $k_w = 0.1$.

By using the adaptive controller proposed and starting with initial conditions over the trajectory, the tilt-rotor UAV was designated to perform a forward acceleration along the path $x_r(t) = 0.25t^2$, $y_r = 0$, $z_r = 10$ and $\psi_r = 0$ during the first twenty seconds, then do a circular trajectory given by $x_r = r_t cos((2\pi(t+40)/80)) + 100$, $y_r = r_t sin((2\pi(t+40)/80)) + 127.5$, $z_r = 10$ and $\psi_r = (2\pi(t-20)/80)$, with radius $r_t = 127.5m$. A perturbation with respect to inertial axis x was added at time $10s$, as shown in Figure 6.

The results in Figures 3 and 4 show that the tilt-rotor UAV tracks the trajectory x, y, z, ψ maintaining the other states with a small error, even under a time-varying disturbance. The control signals, shown in Figure 5, were maintained bounded.

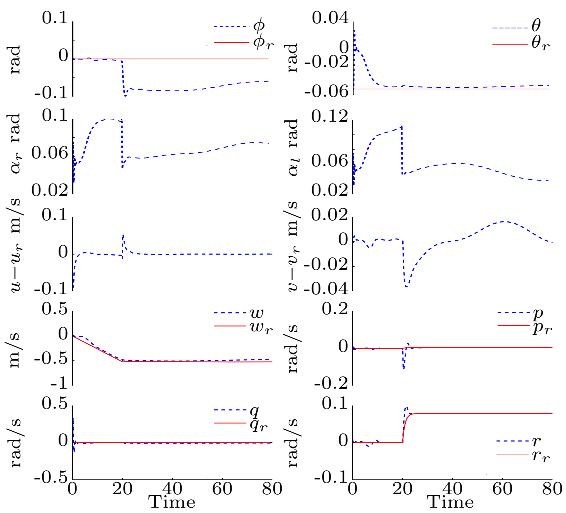

Figure 3: Tilt-rotor states.

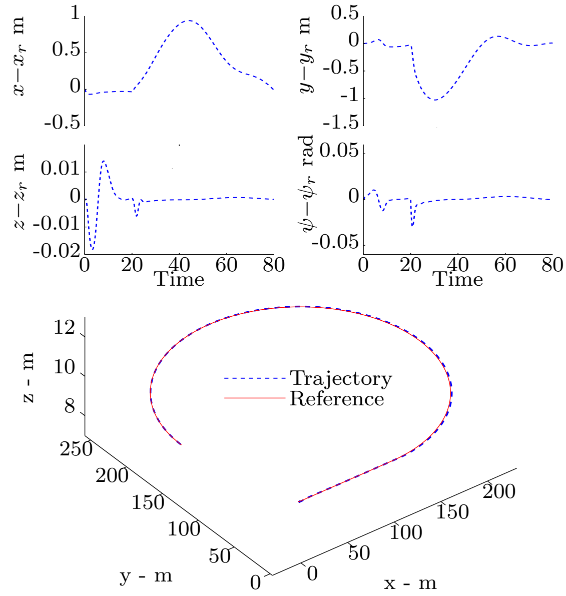

Figure 4: Tilt-rotor tracking error and trajectory.

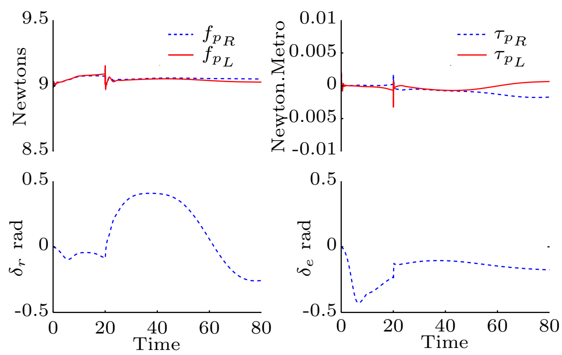

Figure 5: Tilt-rotor control signals.

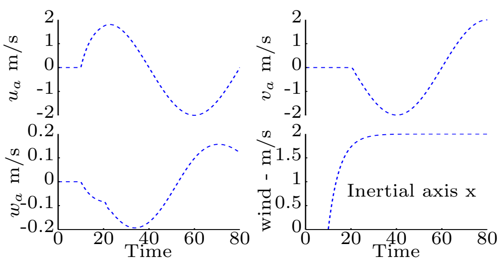

Figure 6: Environment wind disturbance.

5 Conclusions and future works

This works presented the modeling and control of a tilt-rotor UAV with tail control surfaces. Linear state feedback mixed H_2/H_∞ controllers were designed for different operation points, and a gain-scheduling scheme, using neural network, was applied in order to solve the nonlinear control problem. Under numerical simulation it was shown the controller efficiency, when the UAV was designated to perform a forward acceleration followed by a circular trajectory, with a time wind varying perturbation.

Future works include test the controller under real flight experiments to validate the modeling and control efficiency. Furthermore, to improve the energy consumption and, consequently, increase the autonomy, the next step is to design the tilt-rotor UAV with wings and design a controller using a similar approach to solve the problem.

$$\begin{aligned} C_z =& diag(\frac{1}{0.1}, \frac{1}{0.1}, \frac{1}{0.1}, \frac{2}{\pi}, \frac{2}{\pi}, \frac{2}{\pi}, \frac{1}{\pi}, \frac{1}{\pi}, \\ & \frac{1}{0.1}, \frac{8}{\pi}, \frac{8}{\pi}, \frac{4}{\pi}, \frac{8}{\pi}, \frac{8}{\pi}, \frac{1}{0.1}, \frac{1}{0.1}, \frac{1}{0.1}, \frac{1}{0.1}) \end{aligned} \tag{13}$$

$$D_{uz} = \begin{bmatrix} 0.6 & 0.6 & 6 & 6 & 0 & 0 \\ 0.6 & 0.6 & 6 & 6 & 0 & 0 \\ 0.6 & 0.6 & 6 & 6 & 0 & 0 \\ 0.3 & 0.3 & 3 & 3 & 0 & 0 \\ 0.3 & 0.3 & 3 & 3 & 3.6/\pi & 0 \\ 0.3 & 0.3 & 3 & 3 & 0 & 4.8/\pi \\ 0 & 0 & 6 & 0 & 0 & 0 \\ 0 & 0 & 0 & 6 & 0 & 0 \\ 0.6 & 0.6 & 6 & 6 & 0 & 0 \\ 0.6 & 0.6 & 6 & 6 & 0 & 0 \\ 0.6 & 0.6 & 6 & 6 & 3.6/\pi & 0 \\ 0.6 & 0.6 & 6 & 6 & 0 & 10.8/\pi \\ 0 & 0 & 6 & 0 & 0 & 0 \\ 0 & 0 & 0 & 6 & 0 & 0 \\ 0.6 & 0.6 & 6 & 6 & 0 & 0 \\ 0.6 & 0.6 & 6 & 6 & 0 & 0 \\ 0.6 & 0.6 & 0.3 & 0.3 & 0 & 0 \\ 0.6 & 0.6 & 6 & 6 & 0 & 4.8/\pi \end{bmatrix} \tag{14}$$

$$D_{wz} = \begin{bmatrix} 0.2\boldsymbol{I}_{3\times3} & 0.5\mathbf{1}_{3\times3} & 0.1\mathbf{1}_{3\times2} & \mathbf{0}_{3\times10} \end{bmatrix}' \tag{15}$$

Table 1: System Parameters.

Parameter	Value
$\boldsymbol{g}_r'$	$\begin{bmatrix}0 & 0 & -9,8\end{bmatrix}$
β	5 degree
k_τ	1.7e-7
b	9.5e-6
ρ	1.21
s^f, s^h, s^v	$\{0.0146,\ 0.01437,\ 0.013535\}$
$\boldsymbol{d}^{\mathcal{B}}_{c_1}$	$\begin{bmatrix}0 & 0 & 0\end{bmatrix}'$
$\boldsymbol{d}^{\mathcal{B}}_{c_2^{aux}}$	$\begin{bmatrix}0.00498 & -0.27 & 0.0595\end{bmatrix}'$
$\boldsymbol{d}^{c_2^{aux}}_{c_2}$	$\begin{bmatrix}0 & 0 & 0.045\end{bmatrix}'$
$\boldsymbol{d}^{\mathcal{B}}_{c_3^{aux}}$	$\begin{bmatrix}0.00498 & 0.27 & 0.0595\end{bmatrix}'$
$\boldsymbol{d}^{c_3^{aux}}_{c_3}$	$\begin{bmatrix}0 & 0 & 0.045\end{bmatrix}'$
$\boldsymbol{d}^{\mathcal{B}}_{f}$	$\begin{bmatrix}-0.0050 & 0 & 0.0326\end{bmatrix}'$
$\boldsymbol{d}^{\mathcal{B}}_{h}$	$\begin{bmatrix}-0.3858 & 0 & 0.1194\end{bmatrix}'$
$\boldsymbol{d}^{\mathcal{B}}_{v}$	$\begin{bmatrix}-0.3277 & 0 & 0.0288\end{bmatrix}'$
m_{c_1}	1.53116
m_{c_2}, m_{c_3}	0.150
$\boldsymbol{I}_{c_1}$	$\begin{bmatrix}6.635 & 0 & -1.004 \\ 0 & 7.345 & 0 \\ -1.004 & 0 & 8.186\end{bmatrix} 10^{-3}$
$\boldsymbol{I}_{c_2}, \boldsymbol{I}_{c_3}$	$diag(7.7509, 6.9700, 7.6109).10^{-5}$
$c^f_{d_{xz}}(\alpha_a)$	$0.4566\alpha_a^2 - 0.0403\alpha_a + 0.0601$
$c^f_{l_{xz}}(\alpha_a)$	$0.5405\alpha_a - 0.0353$
$c^f_{d_{xy}}(\beta_a)$	$0.3513\beta_a^2 + 0.0604$
$c^f_{l_{xy}}(\beta_a)$	$0.3821\beta_a - 0.0003$
$c^v_{l_{xy}}(\beta_a)$	$-45.392\beta_a^3 + 0.0011\beta_a^2 + 6.1126\beta_a$
$c^v_{d_{xy}}(\beta_a)$	$2.2019\beta_a^2 + 0.0149$
$c^r(\delta_r)$	$2.1873375\delta_r$
$c^h_{l_{xz}}(\alpha_a)$	$-35.216\alpha_a^3 + 6.5306\alpha_a$
$c^h_{d_{xz}}(\alpha_a)$	$1.9382\alpha_a^2 + 0.0088$
$c^e(\delta_e)$	$2.1873375\delta_e$

Acknowledgments

This work was supported by the Brazilian agencies CNPq, CAPES, and FAPEMIG.

References

Almeida, M. M. (2014). *Control strategies of a tilt-rotor uav for load transportation*, Master's thesis, Universidade Federal de Minas Gerais.

Almeida, M. M. and Raffo, G. V. (2015). Nonlinear control of a tiltrotor uav for load transportation, *Prof. of the ACNAAV'15 IFAC*, pp. 232–237.

Beard, R. W. and Mclain, T. W. (2012). *Small unmanned aircraft: Theory and Practice*, Princeton University Press.

Castillo, P., Lozano, R. and Dzul, A. (2005). Stabilization of a mini rotorcraft with four rotors, *IEEE Control Systems Magazine* pp. 45–55.

Donadel, R., Raffo, G. V. and Becker, L. B. (2014). Modeling and control of a tiltrotor uav for path tracking, *Prof. of the 19th IFAC World Congress*, pp. 3839–3844.

Haykin, S. (2001). *Redes neurais: Princípio e prática*, Bookman.

Kane, T. R. and Levinson, D. A. (1985). *Dynamics: Theory and Applications*, Mcgraw-Hill College.

Kendoul, F., Fantoni, I. and Lozano, R. (2005). Modeling and control of a small autonomous aircraft having two tilting rotors, *Prof. of the 44th IEEE Conference on CDC-ECC'05*, pp. 8144–8149.

Nasa (1975). Tilt rotor research aircraft familiarization document, http://ntrs.nasa.gov/archive/nasa/casi.ntrs.nasa.gov/19750016648.pdf.

Norton, B. (2004). *Bell Boeing V-22 Osprey: Tiltrotor Tactical Transport*, Aerofax.

Papachristos, C., Alexis, K., Nikolakopoulos, G. and Tzes, A. (2011). Model predictive attitude control of an unmanned tilt-rotor aircraft, *Prof. of the IEEE ISIE 2011*, pp. 922–927.

Papachristos, C., Alexis, K. and Tzes, A. (2011). Design and experimental attitude control of an unmanned tilt-rotor aerial vehicle, *Prof. of the 15th ICAR 2011*, pp. 465–470.

Raffo, G. V. (2011). *Robust control strategies for a quadrotor helicopter: An underactuated mechanical system*, Master's thesis, Universidad de Sevilla.

Ryan, A. and Hedrick, J. K. (2005). A mode-switching path planner for uav-assisted search and rescue, *Prof. of the 44th IEEE Conference on CDC-ECC'05*, pp. 1471–1476.

Spong, M. W., Hutchinson, S. and Vidyasagar, M. (2006). *Robot Modeling and Control*, Jhon Wiley & Sons, inc.

Stevens, B. L. and Lewis, F. L. (1992). *Aircraft control and simulation*, Wiley-Interscience Publication.